IEEE Access
Multidisciplinary | Rapid Review | Open Access Journal

Received 8 August 2023, accepted 18 September 2023, date of publication 26 September 2023,
date of current version 29 September 2023.

Digital Object Identifier 10.1109/ACCESS.2023.3319433

RESEARCH ARTICLE

SLM Printed Wideband Circularly Polarized Multilayer Antenna Array With Reduced Impact by the Manufacturing Imperfection

HAOYUN YUAN[1], ZHUANGZHUANG LIU[2], LI WANG[3], (Graduate Student Member, IEEE), LIMING SI[1], (Member, IEEE), HOUJUN SUN[1,4], (Member, IEEE), GIOVANNI CRUPI[5], (Senior Member, IEEE), DOMINIQUE SCHREURS[6], (Fellow, IEEE), AND XIUE BAO[1,4], (Member, IEEE)

[1]School of Integrated Circuits and Electronics, Beijing Institute of Technology, Beijing 100081, China
[2]Key Laboratory for Advanced Materials Processing (MOE), Institute for Advanced Materials and Technology, USTB, Beijing 100083, China
[3]School of Electronics and Information Engineering, Xi'an Jiaotong University, Xi'an, Shanxi 710049, China
[4]Tangshan Research Institute, BIT, Tangshan 063000, China
[5]BIOMORF Department, University of Messina, 98125 Messina, Italy
[6]WAVECORE Division of ESAT, KU Leuven, 3001 Leuven, Belgium

Corresponding authors: Zhuangzhuang Liu (liuzhuangzhuang@ustb.edu.cn) and Xiue Bao (xiue.bao@bit.edu.cn)

This work was supported in part by the National Natural Science Foundation of China under Grant 62201037 and Grant 62271056, and in part by the Beijing Institute of Technology (BIT) Youth Academic Start-Up Funding under Grant XSQD-202206001.

ABSTRACT A novel three-dimensional (3-D)-printed wideband circularly-polarized (CP) waveguide based 4 × 4 slotted antenna array is proposed for wireless communications in the paper. For radiating CP waves, several additional eigenmodes are introduced by designing several additional layers. By adjusting the multiple resonances within the cavity, the axial ratio (AR) bandwidth can be enhanced, and the impedance matching can be improved. Due to the good AR performance of the well-designed radiation subarray, the antenna scale can be easily extended by a simple full-corporate-feed network. The multilayered antenna array is fabricated using the cost-effective commercial direct metal laser sintering (DMLS) technology. By incorporating the Huray model, this study considers and simulates the influence of roughness. The antenna has a measured impedance bandwidth of 20.4% (18-22.1 GHz), which is exactly the same as its AR bandwidth. A maximum gain of 21.6 dBic is achieved at 21.3 GHz. It has validated that, compared with state-of-art technologies, the proposed antenna has wide bandwidth and good radiation pattern. The developed antenna shows competitive performance in terms of gain and efficiency with the state-of-the-art antennas. This demonstrates the viability of employing the advanced 3-D printing technique for realizing complex microwave structures, which holds high potential for future wireless communication applications.

INDEX TERMS 3-D printing, antenna array, circularly-polarized, wideband, surface roughness.

I. INTRODUCTION

In order to satisfy the requirements of transmitting data at high speed in common and emerging wireless applications, such as satellite communications and the internet of things (IoT) [1], [2], [3], [4], antennas are in increasing demand to have high-gain, wideband, and high efficiency. Furthermore, in wireless communication systems, circularly-polarized (CP) antennas are attracting increasing attention because, as compared to the linearly polarization antennas, CP antennas have obvious advantage of reducing polarization mismatch and multi-path interference [5], [6]. Due to the characteristics of being lightweight, compact, low-cost, and easy to be integrated, microstrip line [7], [8], [9] and substrate-integrated-waveguide (SIW) based [10], [11] CP antennas are extensively designed for low frequency

The associate editor coordinating the review of this manuscript and approving it for publication was Roberta Palmeri.

communication systems. However, these dielectric substrate based antennas are not recommended for high-frequency systems, as the large dielectric loss usually results in obviously limited radiation efficiency [7], [11]. Thus, it is usually difficult to transmit high power with high efficiency by using the substrate based antennas, especially for large-scale antenna arrays. Therefore, introducing a low insertion loss transmission structure is increasingly necessary to realize a highly efficient wideband CP antenna for high-frequency communication systems.

Considering the excellent characteristics in low insertion loss and high power capability, hollow waveguide based transmission structures are expected to improve the efficiency of large-scale antennas. Hence, some waveguide based high-efficiency antennas have been reported for microwave and millimeter-wave applications [12], [13]. However, these antennas often use the series feeding method [12], [13], thus usually having limited radiation bandwidths because of the long-line effect. Moreover, the distribution of electromagnetic fields and working bandwidths are sensitive to the fabrication tolerance. In order to increase the bandwidth and reduce the frequency dependence of the beam direction, a full-corporate-feed network is introduced to the waveguide antenna arrays for high-frequency wireless communications [14], [15], [16].

In full-corporate-feed network based antennas, multi-layered hollow waveguide based structures, including the radiating layer, the coupling layer, and the feeding layer, are typically designed. The feeding layer, usually consisting of multistage T-junction and H-junction cascades, excites the radiating slots through the coupling layer with equal amplitudes and phases. Though better bandwidth and beam direction are expected for the full-corporate-feed waveguide antennas than the single layer series-feeding ones, it is still challenging to realize a multilayered CP antenna with good performance. The main reason is that the structure of a CP antenna is usually complicated [17], [18], [19], and its bandwidth is often limited by the overlapped bandwidth of the complex impedance matching and the qualified axial ratio (AR).

Using the conventional mechanical processing methods to manufacture the multilayered device is another challenge of the multilayered CP antennas. Considering the complexity of the structure, it is not easy to well control the fabrication precision, even by fabricating the different layers separately. Also, the screw-assisted assembly of the layers can easily lead to distribution variation and even leakage of the electromagnetic fields [15], which can significantly impact the radiation performance and working efficiency of the antenna. To reduce the potential electromagnetic leakage, diffusion bonding of laminated thin-metal-etching plates is used for the multilayered antennas [19], [20]. However, the implementation requirements for this technology are not easy to satisfy, and especially it increases the corresponding fabrication cost. Another effective way to suppress the electromagnetic leakage is to introduce gap waveguides into waveguide antenna arrays [21], [22], [23]. It utilizes a periodically structured metal pins to form an electromagnetic band gap (EBG) to prevent electromagnetic leakage without physical contact. The metal pins can also enhance the operation bandwidth. However, inevitably, the additional metal pins can result in challenges in accurate fabricating.

In this paper, a novel 4 × 4 multilayered CP antenna array operating at 20 GHz is developed. For the proposed CP antenna, two pairs of degenerate modes are developed to increase the bandwidth as opposed to conventional approaches, which only introduce extra resonant frequencies by parasitic layers. A novel design concept based on degenerate modes in a single resonant cavity is utilized. The principle of degenerate mode was validated through parameter analysis, and based on this, the ability to modulate impedance and axial ratio separately was achieved. This provides a reference for similar circular polarization designs in the future. Aiming at manufacturing the complex multilayered antenna in an easy, efficient, and cost-effective way, the direct-metal-laser-sintering (DMLS) additive manufacturing, also known as selective-laser-melting (SLM) 3-D printing technology, is introduced. Though some antennas manufactured by other 3-D printing technologies [24], [25], [26] or DMLS [27], [28] are reported, their structures are generally relatively simple. Fabricating complex multilayered antennas using DMLS is still uncommon, and there is limited research on processing errors, surface roughness, and conductivity encountered during the printing process. This article conducted a detailed study on the effects of above factors during the 3-D printing process, which has significant reference value for future research. The remainder of the paper is organized as follows. In Section II, the design theories and the configuration of the proposed antenna array is described in detail. Section III presents the manufacturing process and working performance of the designed antenna array; a detailed discussion and comparison to the similar antennas with other technologies are also provided. Finally, a conclusion is drawn.

II. DESIGN OF THE ANTENNA ARRAY

Fig. 1 presents the overall metal configuration of the proposed 4 × 4 CP antenna array. From the feeding port to the radiation aperture, there are mainly the feeding part, the radiation part, and the parasitic part, being denoted by Part1, Part2, and Part3, respectively. In Part1, there is a 1-to-4 ways corporate feeding circuit, which is mainly composed of a WR-51 waveguide port and several T-junction power dividers. There are 2 × 2 uniform coupling slots above the power dividers for transmitting electromagnetic waves. The back cavity is designed upon the slots for Part1 to equally equalize the energy from the coupling slots and to excite the radiation slots in Part2. The upper hexagonal aperture of Part2 is particularly designed, so that the electromagnetic waves can be transmitted in a pair of degenerate modes to Part3, eventually being synthesized into CP waves and radiated to

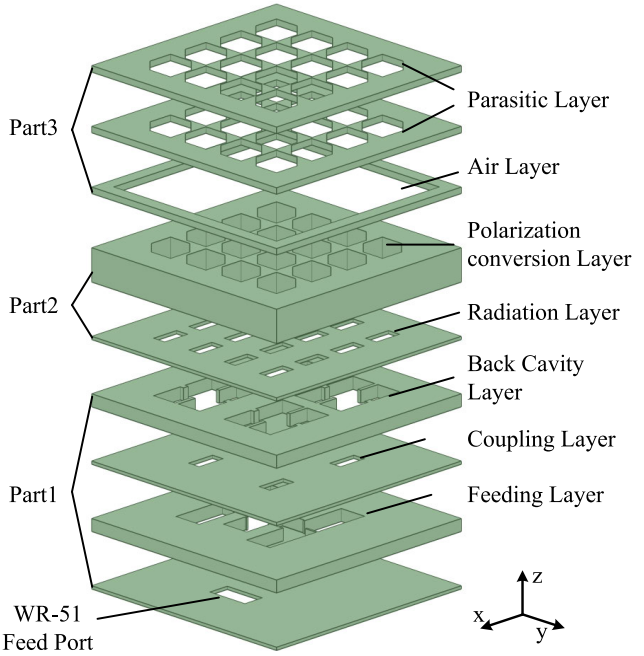

FIGURE 1. Exploded view of the overall circularly-polarized 4 × 4 slot antenna array.

the parasitic slots. The structure and dimensions of Part3, including the simple air gap layer, are carefully designed to expand the AR bandwidth of the final antenna.

A. CP REALIZATION OF THE 2 × 2-ELEMENT SUBARRAY

The proposed antenna array is fundamentally designed based on four 2 × 2 basic radiating element subarrays. Fig. 2(a) schematically presents the metal configuration of the subarray, where the gray areas show the transmission and radiation paths of the electromagnetic fields. Clearly, the basic radiating unit consists of eight homocentric components, i.e., the layers of feed network and coupling slot (Fig. 2(b)), the layers of back cavity and radiation slots (Fig. 2(c)), the layers of hexagonal apertures and air gap (Fig. 2(d)), and the two parasitic slot layers (Fig. 2(e)). Compared to Fig. 1, it is seen that the element subarray starts from a quarter of the feeding layer in Part1. Detailed dimensions and relative locations of the different layers are also provided in Fig. 2.

It is primarily assumed that the electromagnetic waves transmitted by the four radiation slots have identical magnitudes and phases. Hence, to avoid grating lobes within the desired 20% frequency band, the slot distance is designed less than one free-space wavelength at the highest operating frequency. As a result, for an wideband antenna working at the center frequency of 20 GHz, the period distance is designed as 13 mm. Next, the linearly polarized electromagnetic waves are required to be transformed to CP waves. Therefore, four hexagonal apertures are firstly designed to work at the degenerate modes of TE_{101} and TE_{011}, so that two orthogonal electric fields that have equal

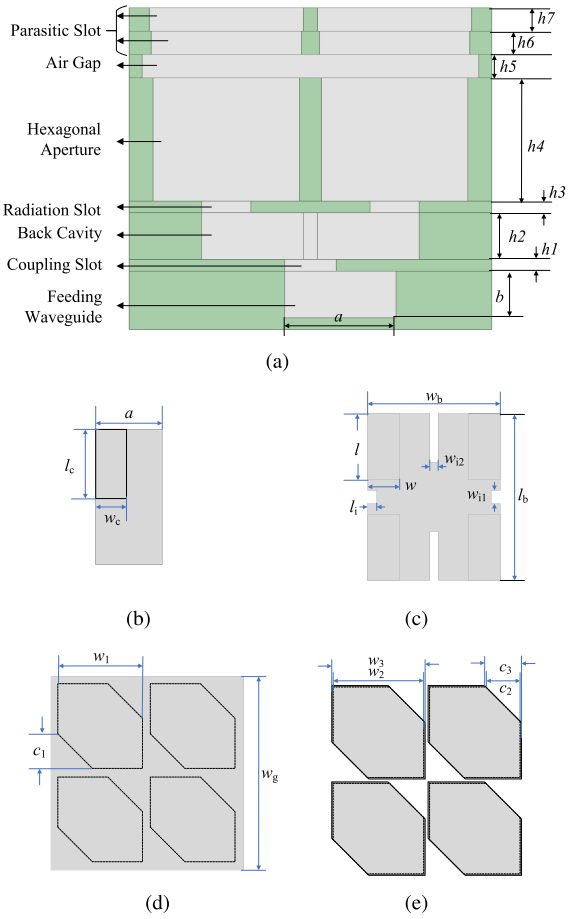

FIGURE 2. (a) Schematic side view of the 2 × 2 element subarray and the schematic top views of (b) the feeding and coupling layers, (c) the cavity and radiation layers, (d) the hexagonal aperture and air gap layers, and (e) the two parasitic slot layers.

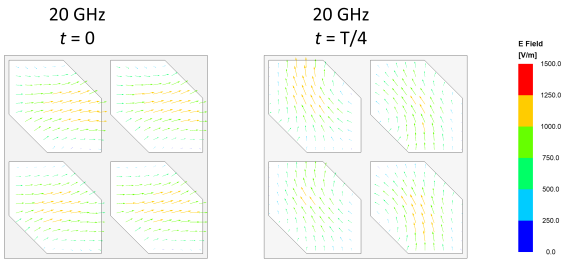

FIGURE 3. Electric field distribution inside the hexagonal aperture at different time.

amplitudes and 90° phase difference can exist. Thus, the square aperture dimension w_1, as shown in Fig. 2(d), can be calculated by

$$f_{\mathrm{TEmn1}} = \frac{c}{2}\sqrt{\left(\frac{m}{w_1}\right)^2 \left(\frac{n}{w_1}\right)^2 \left(\frac{1}{h4}\right)^2} \tag{1}$$

where f_{TEmn1} is the desired center frequency 20 GHz. Next, the square apertures are further designed with a tangential angle for realizing the CP. Fig. 3 presents the electric field distribution inside the hexagonal aperture at the center

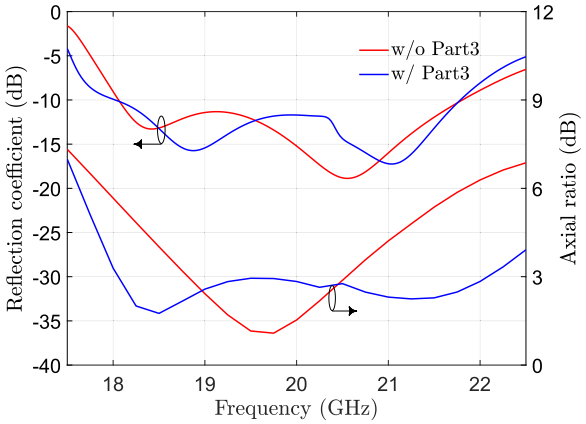

FIGURE 4. Effect of the parasitic layer on impedance matching.

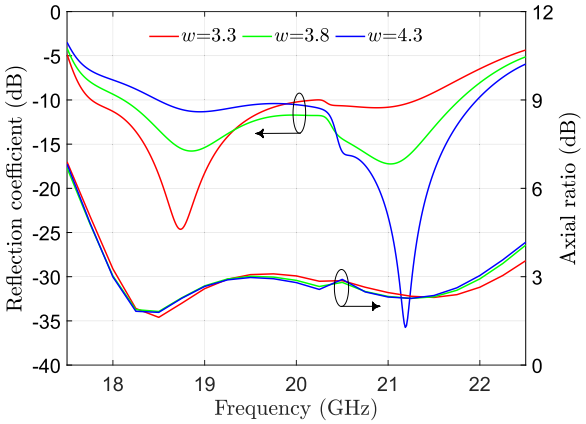

FIGURE 5. Effect of the slot width w on impedance matching and axial ratio.

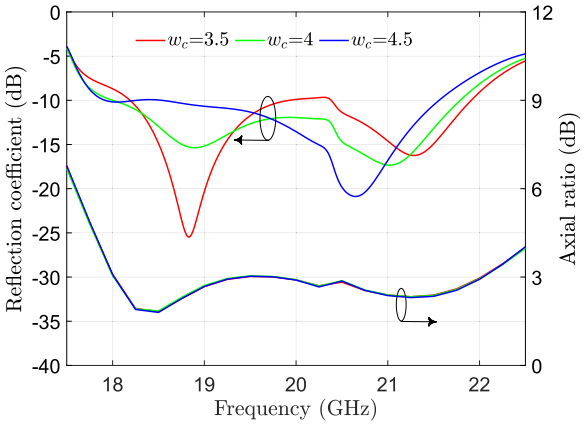

FIGURE 6. Effect of the slot width w_c on impedance matching and axial ratio.

frequency at different time. The electric field distribution within the four apertures is almost identical, with slight amplitude differences due to the non-uniform feeding of the lower structure. It is seen that the electric field at t = 0 has a 90° difference compared to that at t = T/4, with the polarization rotates in a counterclockwise direction, which indicates that the structure can generate a right-hand circular polarization (RHCP).

Aiming at increasing the operating bandwidth, the air gap layer and the two parasitic slot layers (i.e., Part3) are designed. The different widths of w_2, w_3, c_2, and c_3 in Fig. 2(e) are carefully designed to be a two-stage impedance transformer. The dimension of the air layer (w_g) should also be adjusted accordingly. The center positions of the parasitic slot layers are the same as that of the hexagonal aperture layer, and all apertures are equally spaced along the x-axis and y-axis directions. Adding Part3 can also introduce additional eigenmodes at low frequencies [19], which can further effectively help expand the AR bandwidth. As shown in Fig. 4, before adding Part3, the reflection coefficient $|S_{11}|$ of the 2 × 2-element subarray is smaller than −10 dB over 17.5% of the bandwidth ranging from 18.2 GHz to 21.7 GHz; while the bandwidth with the Part3 has increased to 19.1% from 18.0 GHz to 21.8 GHz. The variation of the resonant frequency as shown by the reflection coefficient indicates that additional eigenmodes are added by introducing the Part3. The AR shown in Fig. 4 indicates that the AR bandwidth is enhanced from 9.1% (from 18.8 GHz to 20.6 GHz) to 20% (from 18 GHz to 22 GHz) due to the introduction of Part3.

B. FEED NETWORK OF THE 2 × 2-ELEMENT SUBARRAY

Fig. 2(b) and (c) present the structures and dimensions of the feed network for the 2 × 2 subarray. The back cavity layer beneath the radiation slots layer is designed at its dominant mode. As shown in Fig. 2(c), the two pairs of metal walls are designed to suppress unwanted high-order modes. Due to the dominant mode, the electromagnetic field in the cavity is symmetrically distributed so that a uniform excitation at the radiation slots can be realized. Thus, the electromagnetic waves radiated by the four radiation slots in Part2 have the same magnitudes and phases. The coupling slot is placed at the center beneath the back cavity, as shown in Fig. 2(a) and (b). In order to realize a strong excitation in the back cavity, the coupling slot has an offset of 0.5a from the center axis of the waveguide in feed network layer. As shown in Fig. 2(b), the outer edges of the the coupling slot and the feeding waveguide are in good alignment so that the coupling power can be maximally transmitted. For low profile design, the width a and b length of the feeding waveguide in Fig. 2(b) is designed as 8.6 mm and 3.6 mm, respectively. Then the cutoff frequency of the subarray is 17.4 GHz.

The dimensions of the radiation slot, the back cavity, and the coupling slot are particularly further optimized to realize a good impedance matching. The impacts on the reflection coefficient and the AR caused by the variations of the radiation slot width w and the coupling slot width w_c are respectively presented in Figs. 5 and 6. It is shown the two dimensions mainly affect the depth and position of the $|S_{11}|$ resonance point, but have almost no effect on the amplitude and bandwidth of the AR. Actually, the effect of the other dimensions of the radiation slot, the back cavity,

TABLE 1. Dimensions of The 2 × 2-Element subarray (Unit: mm).

b	$h1$	$h2$	$h3$	$h4$	$h5$	$h6$	$h7$
3.6	0.9	3.6	0.9	9.5	1.8	1.8	1.8
a	l_c	w_c	l	w	l_b	w_b	l_i
8.6	8.93	3.98	8.55	3.8	21.55	17.14	1.18
w_{i1}	w_{i2}	w_1	c_1	w_2	c_2	w_3	c_3
1.72	1.09	11.3	3.58	11.6	4.8	11.9	4.41

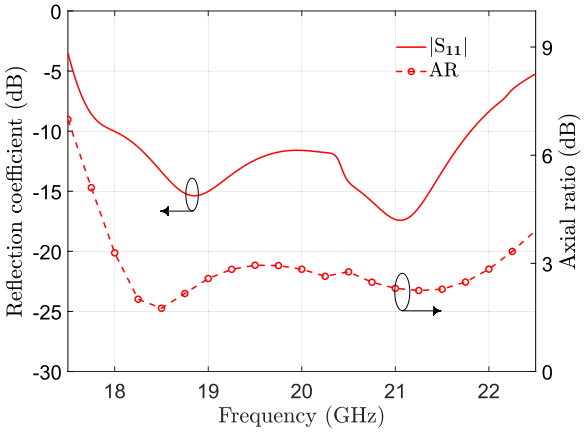

FIGURE 7. Frequency dependence of the reflection coefficient and the axial ratio of the 2 × 2 subarray.

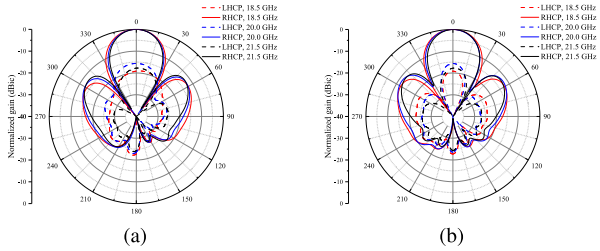

FIGURE 8. The radiation pattern of the subarray at 18.5 GHz, 20 GHz, and 21.5 GHz, respectively in (a) *xoz* plane and (b) *yoz* plane.

and the coupling slot is the same. This phenomenon indicates that their effect on each characteristic mode is the same. Therefore, the impedance matching and axial bandwidth of the CP slot antenna can be optimized separately. The corresponding final dimensions of Fig. 2 are listed in detail in Table 1.

The 2 × 2 subarray of Fig. 2 is analyzed by using the full-wave finite-element-simulation method. Fig. 7 shows the simulated reflection coefficient and axial ratio within the frequency from 17.5 GHz to 22.5 GHz. According to Fig. 7, the simulated bandwidth of the proposed subarray for $|S_{11}|$ smaller than −10 dB is 19.1% (from 18.0 to 21.8 GHz). While the AR bandwidth defined by AR < 3 dB is 20.9% (from 18.0 GHz to 22.2 GHz). Therefore, the overlapping bandwidth of the optimized subarray is 19.1% from 18.0 GHz to 21.8 GHz for the RHCP. Fig. 8 presents

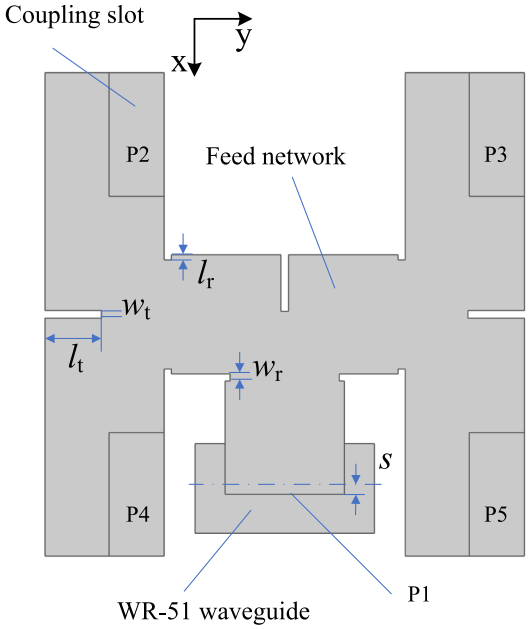

FIGURE 9. Top view of the feed network (l_t = 4.09, w_t = 0.54, l_r = 0.36, w_r = 0.52, w_t = 0.54, s=0.42, unit: mm).

its radiation patterns at 18.5 GHz, 20 GHz, and 21.5 GHz in two orthogonal planes. It indicates that the RHCP is stable and symmetrical within the operating band. Moreover, the sidelobe level is about −13 dB and the cross-polarization level is better than −15 dB.

C. FEED NETWORK OF THE CP ANTENNA ARRAY

Based on the basic subarray, a wideband 4 × 4 CP slot antenna array is further designed for higher-gain radiation. The 4 × 4 slot antenna array is operated under the same working principle as the 2 × 2-element CP slot antenna in Fig. 2. As the AR bandwidth of the subarray can fully cover the impedance bandwidth, only a symmetric and simple feed network without involving any complex sequential rotation technologies [23] is designed. Fig. 9 presents the designed 1-to-4 ways two-stage T-junction structure, where no offset is used in the metal septum, so that the amplitude and phase at each port of the T-junction are identical. The size and dimensions of the septum (l_t, w_t) and iris (l_r, w_r) are carefully adjusted and optimized so that a good impedance matching can be achieved. Moreover, the standard WR-15 aperture cannot be directly connected to the trunk of the first T-junction, as this leads to severe reflection of the transitional section. A certain offset s is thus required for impedance matching. The simulated S-parameters of the 1-to-4 power divider from 17.5 GHz to 22.5 GHz are shown in Fig. 10. Within the entire frequency range, the reflection coefficient is less than −15 dB, and within the desired frequency range of 18 GHz to 22 GHz, it is further below −20 dB. In addition, the magnitude and phase differences between each port are smaller than 0.18 dB and 1.02°, respectively. When designing

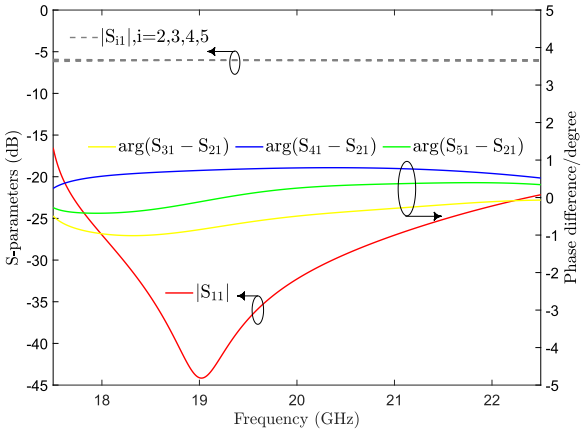

FIGURE 10. Phase difference and power ratio of the 1-to-4 ways feed network.

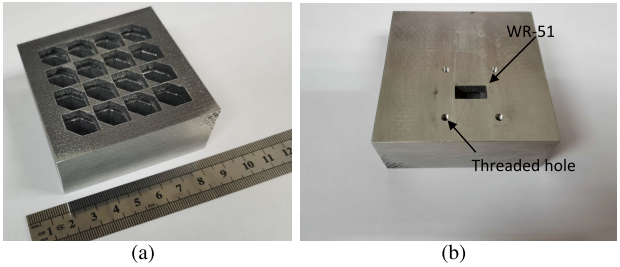

FIGURE 11. (a) Top view and (b) bottom view photographs of the fabricated 3-D printed antenna array.

the 4 × 4 CP slot antenna array based on the subarray, the air gap layer needs to be appropriately adjusted to achieve a good radiation mode and AR. Besides, the dimensions of parasitic slots also need to be adjusted accordingly. The overall configuration of the proposed antenna is finally of $4.53\lambda_0 \times 4.53\lambda_0 \times 1.96\lambda_0$, where the λ_0 is the wavelength of the center frequency 20 GHz.

III. ANTENNA FABRICATION AND CHARACTERIZATION

The designed multilayered structure described in the previous section was manufactured using commercial DMLS technology, and all layers were printed as a whole to reduce electromagnetic leakage. The aluminium-based alloy powder AlSi10Mg is selected as the manufacturing material, due to its good electrical conductivity (about 25%IACS (International Annealing Copper Standard) as manufactured and 45%IACS (2.61 × 10^7 S/m) with stress relief and T6 heat treatments), good corrosion resistance, high dynamic toughness, and excellent thermal conductivity ($170 \pm 10\ Wm°C$). Fig. 11 presents the fabricated device, with a fabrication tolerance of 0.1 mm. After the DMLS process, four blind threaded holes were carefully drilled for connecting the WR-51 feeding waveguide by means of screws. The surface was polished so that very good alignment can be realized to reduce electromagnetic wave leakage. Other than that, there was no further stress relief, heat treatment, or ball-milling treatment

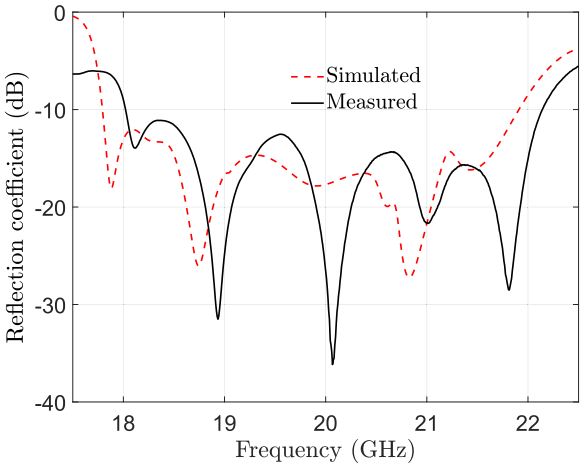

FIGURE 12. Simulated and measured reflection coefficients of the multilayered antenna array within the frequency range from 17.5 GHz to 22.5 GHz.

to the device. The total size of the antenna array is 68 mm × 68 mm × 29.5 mm (including 4.6 mm flange layer) and the aperture size is 51.6 mm × 51.6 mm.

A. REFLECTION COEFFICIENT

In order to analyze the working bandwidth of the antenna array, its reflection coefficient is firstly measured. The results at 801 frequency points within the frequency range from 17.5 GHz to 22.5 GHz are recorded using the Agilent vector network analyzer (VNA) E8363B. The measured reflection coefficient $|S_{11}|$ of the 4 × 4 array is plotted in Fig. 12. For comparison, the simulation results at the same frequencies is also presented in Fig. 12. For the impedance bandwidth that is defined by $|S_{11}| < -10$ dB, it is about 20.4% (from 18 to 22.1 GHz) for the measured result and about 20% (from 17.8 to 21.9 GHz) for the simulated result. There is a slight deviation between the measured and simulated bandwidths, and the measurement moves toward high frequencies. This deviation might be related to manufacturing tolerance of the DMLS technology, especially the dimensional deviation a of the feed network.

Considering the 0.1 mm manufacturing error, mainly the dimension a at the feeding part of the simulated device is reduced or increased 0.1 mm, respectively. For comparison, all the air dimensions in Part1 and the radiation slot with 0.1 mm reduction are also simulated. The corresponding reflection coefficients under the three conditions are both plotted, together with the measured result, in Fig. 13. It is shown that when the dimension a at the feeding part is reduced by 0.1 mm, the simulated $|S_{11}|$ has better agreements with the measurement result. And when considering all the dimensions, the simulation is closer. This dimensional error may be due to the fact that the printed metal surface is not smooth enough, resulting in a slightly smaller hollow feed network in the actually obtained device. It should also be noted that the cutoff frequency of the device is

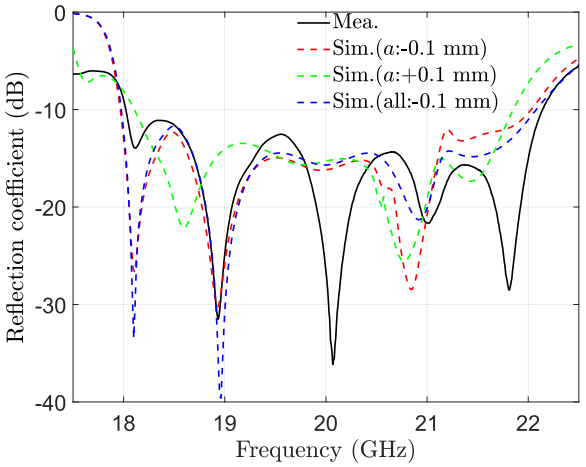

FIGURE 13. Influence of size error in feed network and others on reflection coefficient.

about 17.4 GHz, due to waveguide dimension of a in the feed network. The practically narrower feeding waveguide can lead to the increase of the cutoff frequency to about 17.6 GHz for $a - 0.1mm$. This might explain the obvious frequency shift of $|S_{11}|$ within the operating band. It is worth reminding that other influences, such as assembly tolerance and measurement error, might also contribute to the inconsistency between measurement and simulation. All in all, according to the above analysis, the inconsistency is mainly caused by the dimensional error of the feed network.

B. RADIATION PATTERN AND EFFICIENCY

The antenna array was then measured in microwave anechoic chamber based on a far-field test program. In order to obtain the radiation patterns of the CP antenna array, a standard short waveguide probe is connected to the VNA and used as the signal transmitting port. Electromagnetic waves are emitted through the short waveguide, and received by the antenna device under test, which is connected to the other port of the VNA. The standard waveguide probe is installed for the horizontal polarization and vertical polarization, respectively. For each polarization, the amplitudes and phases of the electric fields in *xoz*-plane and *yoz*-plane are measured, respectively. Next, the RHCP and LHCP radiation patterns are obtained by synthesizing the measured amplitudes and phases in the two orthogonal directions (E_θ, E_φ) by [23]

$$\vec{E}_{RHCP} = (\vec{E_\theta} \; j\vec{E_\varphi})\sqrt{2} \tag{2}$$

$$\vec{E}_{LHCP} = (\vec{E_\theta} \; -j\vec{E_\varphi})\sqrt{2} \tag{3}$$

Fig. 14(a) to 14(f) present the measured and simulated normalized radiation patterns of the proposed antenna at 18.5 GHz, 20 GHz, and 22 GHz, respectively. Generally, for both the RHCP and LHCP, the measured radiation patterns are in very good agreements with the simulation results, with the cross-polarization smaller than −15 dB at the three selected frequencies in Fig. 14. In addition, the radiation patterns at the three frequencies are in very good consistency, which indicates the stable radiation performance of the antenna in the working bandwidth. It is seen that the first sidelobe level is about −12 dB, which is as expected since the amplitude and phase of the electromagnetic waves at each radiation slot are the same [27]. However, there is a slight asymmetry in the side lobes, especially at 18.5 GHz in Fig. 14(a). This might be related to the potential inclination of the radiation aperture caused by the manufacturing process, as the device is manufactured in an angle of 45° with a support structure beneath it.

Based on the measured amplitudes and phases in the two orthogonal directions, the measured AR can also be obtained, which is depicted in Fig. 15. For comparison, the simulated AR within the bandwidth is also added in Fig. 15. Notably, the measured AR is in very good consistency with the simulated results, with the plots overlapping with each other. This also indicates that the structural dimension error below the hexagonal aperture layer has minimal impact on the AR, as has been explained earlier. The measured and simulated AR bandwidth of AR < 3 dB are both 18 GHz to 22.1 GHz, which is perfectly in agreement with the measured impedance bandwidth.

The linearly polarization gains of the antenna in the two orthogonal directions are further measured based on the gain-comparing method. Then the total gain of the CP antenna array can by obtained by combining the two linearly polarization gains. The measured peak gain is presented in Fig. 16, where the simulated gain is also added. It is clear that the maximum peak gain is 21.6 dBic at 21 GHz. At the center frequency 20 GHz, the realized gain is 20.4 dBic, 1.2 dB smaller than the maximum value at 21 GHz. Over the major portion of desired frequency range, the peak gain is at least 18 dBic, in average 1.2 dB lower than the simulation. This small discrepancy can be partly related to extra power loss that is caused by surface roughness and discontinuity between the antenna and the connecting port, due to errors in the 3-D printing process and the assembly imperfection. It is noted that there is a big difference between the measured and the simulated gains at low frequencies. At 18 GHz, the measured gain is only about 16 dBic, about 3 dB lower than the simulated result. This difference at low frequencies might be related to the variation of the cutoff frequency of the antenna. As mentioned above, the interior dimensions of the manufactured device are slightly smaller than the design, leading to the increase of its cutoff frequency. While as the cutoff frequency of the device is close to 18 GHz, the increase of the cutoff frequency can inevitably affect the radiation performance.

According the obtained gain, the efficiency of the CP antenna can be calculated by [23]

$$\eta_{mea_{ap}} = \frac{G_{mea}c^2}{f^2 4\pi A} \tag{4}$$

where c is the free space velocity, f is the frequency at which the maximum measured gain G_{mea} is obtained, and A is the radiation aperture area of the antenna. Thus, for a

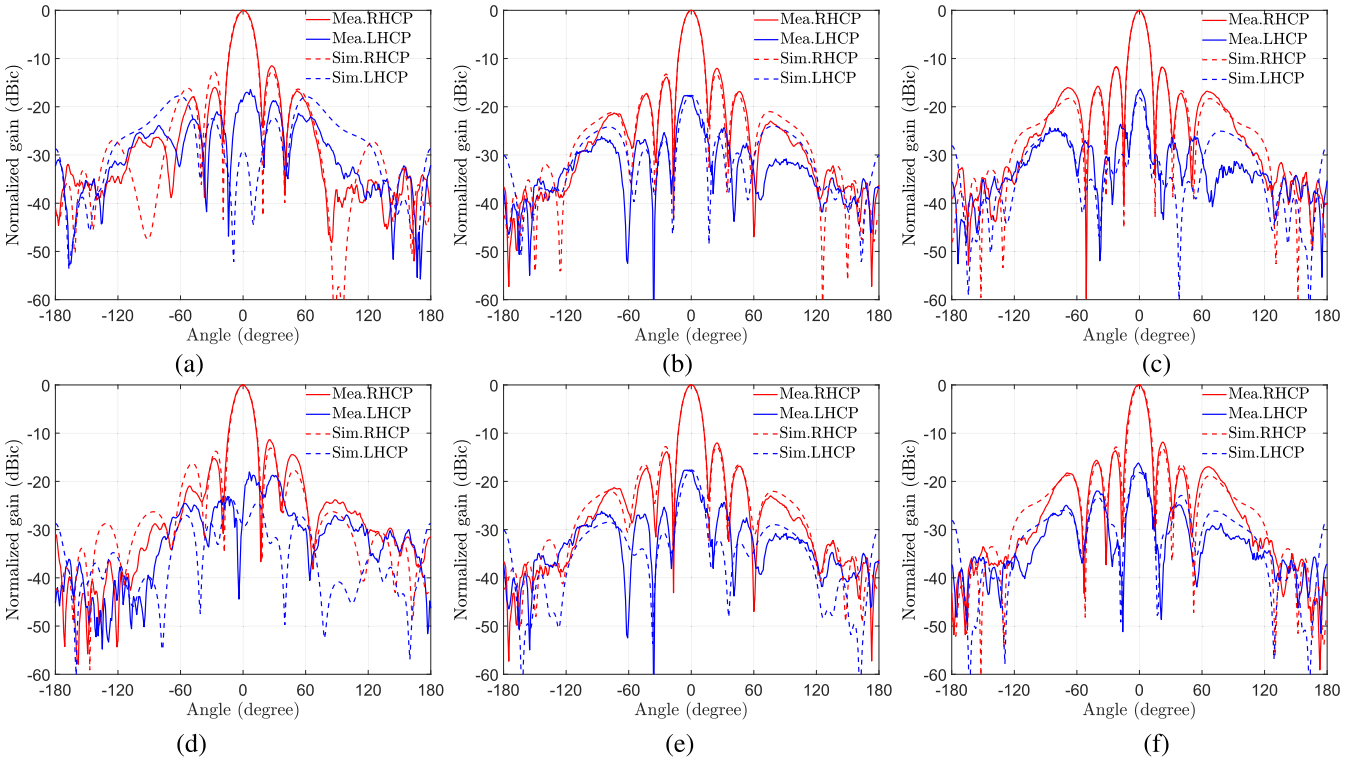

FIGURE 14. Measured and simulation radiation patterns of the 3-D printed antenna: (a) *xz*-plane at 18.5 GHz, (b) *xz*-plane at 20 GHz, (c) *xz*-plane at 22 GHz, (d) *yz*-plane at 18.5 GHz, (e) *yz*-plane at 20 GHz, and (f) *yz*-plane at 22 GHz.

TABLE 2. Comparison of previously reported antenna arrays and this work.

Ref.	Antenna catagory	f_0 (GHz)	BW (%)	Peak gain (dBic)	Total efficiency (%)	Array scale	Size* (normalized to λ_0)
[8]	Microstrip line (PCB)	28.35	14.0	18.2	56.0	4 × 4	3.02 × 3.02 × 0.21
[9]	Microstrip line (PCB)	14.5	4.2	15.2	30.2	4 × 4	3.65 × 2.30 × 1.01
[10]	SIW (PCB)	59	16.6	20	52.4	4 × 4	3.32 × 3.32 × 0.48
[11]	SIW (PCB)	19.9	13.8	25.9	25.9	16 × 16	10.6 × 10.6 × 0.13
[17]	Air-filled waveguide (Milling)	17	7.0	15.4	94.0	1 × 4	0.86 × 3.43 × 4.53
[18]	Air-filled waveguide (Milling)	30	16.0	32.8	98.9	16 × 16	12.9 × 12.9 × 5.1
[19]	Air-filled waveguide (Diffusion bonding)	60	~3.0	32.7	75.5	16 × 16	13.6 × 13.6 × 1.0
[23]	Ridge gap waveguide (Milling)	31	20.0	26.5	84.9	8 × 8	6.61 × 6.61 × 1.71
This work	Air-filled waveguide (3-D printing)	**20**	**20.5**	**21.6**	**88.2**	**4 × 4**	**3.39 × 3.39 × 1.66**

BW: $|S_{11}|$ < -10 dB and AR < 3 dB. * Size is the aperture and profile dimensions: Length × Width × Height.

certain working bandwidth, the antenna efficiency is mainly determined by the gain. According to Fig. 16, the antenna efficiency values at 60%, 70%, 80%, 90% and 100% are respectively presented in Fig. 16, by plotting the measured peak gain as a function of frequency. Notably, the measured efficiency is at least 50% from 18 GHz to 22.1 GHz, covering the complete working bandwidth of the antenna. At the center frequency 20 GHz, the efficiency is 73.7% and at the frequency of 21 GHz, the antenna efficiency can be as high as 88.2%. Unfortunately, it is still clear that at low frequencies, there is a big difference between the measured efficiency and the simulated results.

The difference in efficiency might firstly be related to the obvious gain decrease caused by the variation of the cutoff frequency. Therefore, the 4 × 4 array with slightly narrowed feeding waveguide (dimensions −0.1 mm) is simulated and the obtained result is provided in Fig. 16. Moreover, surface roughness of 3-D printed structures might also affect the performance of microwave devices [24]. In order to analyze the impact of surface roughness, the Huray model is introduce [29], in which conducting spheres are stacked on a flat conductor surface to illustrate the relationship between roughness and equivalent conductivity. Due to the surface roughness, the equivalent conductivity of the ALSi10Mg is modified by [30]

$$\sigma'(f) = \frac{\sigma}{K_s(f)^2} \tag{5}$$

where σ is the constant conductivity ($\sigma = 2.0 \times 10^7$ S/m for ALSi10Mg), $\sigma'(f)$ is the equivalent conductivity considering

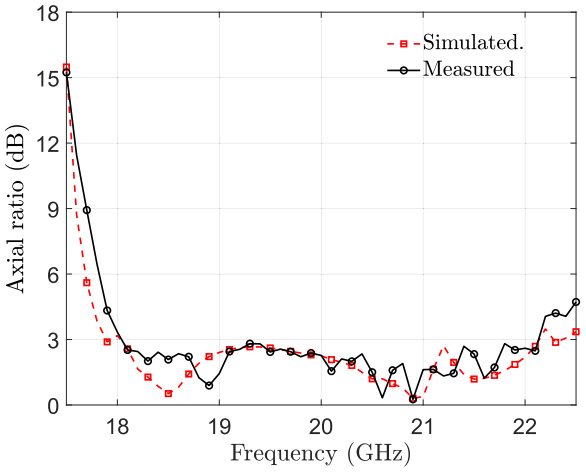

FIGURE 15. Simulated and measured AR of the 3-D printed antenna.

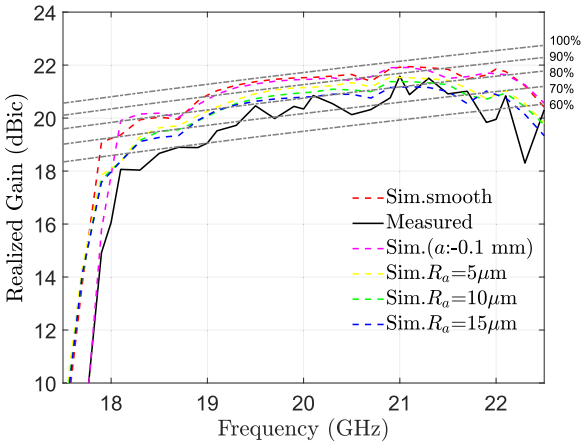

FIGURE 16. Peak realized gain by considering feeding waveguide dimension various RMS surface roughness values.

the the surface roughness, and $K_{ch}(f)$ is the cannonball-huray roughness correction factor, which is calculated with the 14 snowballs' model by [29]

$$K_{CH}(f) = 1 \ \frac{7}{3}\pi(1 \ \frac{\delta(f)}{r} \ \frac{\delta^2(f)}{2r^2})^{-1} \tag{6}$$

where $\delta(f)$ is the skin depth as a function of frequency and r is the radius of the balls, which is related to roughness parameters R_a through $R_a \times 2 \times \sqrt{3} = r0.06$. The roughness parameter of the DMLS 3-D printing method herein used is about 6 μm to 10 μm. Thus, to observe the impact of various roughness values on gain, the simulated results when R_a is 5 um, 10 um, and 15 um are also added in Fig. 16. As show in Fig. 16, the surface roughness indeed can affect the performance of the 3-D printed antenna, while the difference between different roughness parameters is not significant. Due to the additional conductive loss caused by surface roughness, the peak gain is reduced by approximate 0.8 dB for the three cases, very close to the measurement results. It can be also seen in Fig. 16 that, as expected, the fabrication tolerance mainly affect the peak gain at low frequencies. The decease of peak gain at low frequencies further leads to the decrease of the antenna efficiency to a value very close to the measurement result.

C. COMPARISON AND DISCUSSION

A comparison between the proposed antenna array and state-of-art CP antennas is summarized in Table 2 to evaluate the performance of the 3-D printed antenna. Both planar and 3-D designs are considered. The designs with a microstrip-line or a SIW feed network are realized using single layered or multilayered PCB facilities, whereas waveguide arrays are entirely metallic structures produced using milling, diffusion bonding, or 3-D printing technologies. The designed center frequency, working bandwidth, array scale, peak gain, total efficiency, and the overall size are carefully compared. As the antenna efficiency is not reported in some literature, it is calculated according to (4) by using the frequency f_0, the aperture dimension, and the measured maximum gain.

It can be seen that the microstrip or SIW based antennas have great advantages in low profile, while their working bandwidths are relatively narrow. Moreover, the planar antennas with dielectric layers have a much smaller total efficiency than the fully metallic 3-D structures. Especially, for a large-scale array [11], its total efficiency is only 25.9%, much smaller than other waveguide antenna arrays. This indicates that at high microwave frequencies, the influence of dielectric loss on the final performance of an antenna cannot be ignored. It can be validated by the fact that, compared with the above antennas, the 3-D antennas that are manufactured by using the milling or the diffusion bonding methods can achieve higher gain and total efficiency. However, it is validated by Table 2 that, when only single layer radiation aperture is used, the bandwidth is still less than 20% [17], [18]. Using the parasitic radiation apertures can enhance bandwidth, nevertheless, have the challenges of manufacturing, which may result in much worse actual performance than the corresponding simulation results [19]. Sequential rotation technology can also expand AR bandwidth, so that [23] achieves 20% bandwidth. However, the sequential phase of the power dividers outputs is disturbed by changing the frequency. Therefore, additional gain drop is inevitable, except at the center frequency.

It can be further seen from Table 2 that the proposed antenna array can achieve relatively widest bandwidth by multiple pairs of degenerate modes. Utilizing DMLS 3-D printing technology not only mitigates the effects of manufacturing imperfections but also contributes to lower manufacturing costs. Nevertheless, compared to the antennas fabricated by using diffusion bonding and milling technologies, the proposed antenna is not outstanding in efficiency. This is mainly related to the surface roughness and the manufacturing tolerance related to the DMLS 3-D printing process. The effect of surface roughness can be reduced by introducing a post-processing, such as mechanical or chemical polishing, while the manufacturing tolerence can be considered when designing the devices. Generally, the performance of the proposed design is still outstanding,

which demonstrates the feasibility of the DMLS 3-D printing technology in fabricating high-frequency microwave antennas.

IV. CONCLUSION

A full-corporate-feed waveguide network based wideband CP antenna array was designed for working at the center frequency of 20 GHz. By using the DMSL addictive manufacturing technology, a 68 mm × 68 mm × 29.5 mm antenna was fabricated. Parasitic slots were designed to expand the AR bandwidth by introducing additional eigenmodes, reaching a much wider AR bandwidth of 20.5%, which was also completely overlapping with its impedance bandwidth. The measured total efficiency at the working frequency range exceeded 50%, with a peak gain of 21.6 dBic at 21 GHz. Although the measured gain was slightly affected by the roughness of the DMSL 3-D printing technology, the proposed antenna still has shown significant advantages compared to the existing antennas, including the performance and the fabrication cost. The measurement results fully demonstrated the great potential and advantages of the emerging 3-D printing antenna with complex structures, which shows that the propose antenna is a promising candidate for communications.

ACKNOWLEDGMENT

The authors would like to thank the University of Science and Technology Beijing for post-processing of the 3D-printed antenna.

REFERENCES

[1] O. Kodheli, E. Lagunas, N. Maturo, S. K. Sharma, B. Shankar, J. F. M. Montoya, J. C. M. Duncan, D. Spano, S. Chatzinotas, S. Kisseleff, J. Querol, L. Lei, T. X. Vu, and G. Goussetis, "Satellite communications in the new space era: A survey and future challenges," *IEEE Commun. Surveys Tuts.*, vol. 23, no. 1, pp. 70–109, 1st Quart., 2021.

[2] M. Ferrando-Rocher, J. I. Herranz-Herruzo, A. Valero-Nogueira, and B. Bernardo-Clemente, "Dual circularly polarized aperture array antenna in gap waveguide for high-efficiency Ka-band satellite communications," *IEEE Open J. Antennas Propag.*, vol. 1, pp. 283–289, 2020.

[3] L. Chettri and R. Bera, "A comprehensive survey on Internet of Things (IoT) toward 5G wireless systems," *IEEE Internet Things J.*, vol. 7, no. 1, pp. 16–32, Jan. 2020.

[4] D. C. Nguyen, M. Ding, P. N. Pathirana, A. Seneviratne, J. Li, D. Niyato, O. Dobre, and H. V. Poor, "6G Internet of Things: A comprehensive survey," *IEEE Internet Things J.*, vol. 9, no. 1, pp. 359–383, Jan. 2022.

[5] J.-Y. Deng, C.-L. Lou, Z. Chen, and Y. Zhang, "Circularly polarized horn antenna with miniaturized longitudinal dimension for vehicular satellite communications," *IEEE Trans. Veh. Technol.*, vol. 72, no. 4, pp. 5497–5501, Apr. 2023.

[6] E. Kang, T. H. Lim, and H. Choo, "Design of a circularly polarized high-gain patch antenna using a higher-order mode with a heterogeneous substrate layer for GPS applications," *IEEE Access*, vol. 11, pp. 79224–79231, 2023.

[7] J. Huang, "A Ka-band circularly polarized high-gain microstrip array antenna," *IEEE Trans. Antennas Propag.*, vol. 43, no. 1, pp. 113–116, Jan. 1995.

[8] J. Wu, Y. J. Cheng, and Y. Fan, "Millimeter-wave wideband high-efficiency circularly polarized planar array antenna," *IEEE Trans. Antennas Propag.*, vol. 64, no. 2, pp. 535–542, Feb. 2016.

[9] J. Zhu, Y. Yang, S. Li, S. Liao, and Q. Xue, "Dual-band dual circularly polarized antenna array using FSS-integrated polarization rotation AMC ground for vehicle satellite communications," *IEEE Trans. Veh. Technol.*, vol. 68, no. 11, pp. 10742–10751, Nov. 2019.

[10] J. Zhu, S. Liao, S. Li, and Q. Xue, "60 GHz wideband high-gain circularly polarized antenna array with substrate integrated cavity excitation," *IEEE Antennas Wireless Propag. Lett.*, vol. 17, no. 5, pp. 751–755, May 2018.

[11] D.-F. Guan, C. Ding, Z.-P. Qian, Y.-S. Zhang, Y. Jay Guo, and K. Gong, "Broadband high-gain SIW cavity-backed circular-polarized array antenna," *IEEE Trans. Antennas Propag.*, vol. 64, no. 4, pp. 1493–1497, Apr. 2016.

[12] H.-T. Zhang, W. Wang, Z. Zheng, M.-P. Jin, and X.-L. Liang, "A novel dual circularly-polarized waveguide antenna array," in *Proc. IEEE Int. Symp. Antennas Propag. USNC/URSI Nat. Radio Sci. Meeting*, Jul. 2018, pp. 509–510.

[13] J. Tak, A. Kantemur, Y. Sharma, and H. Xin, "A 3-D-printed W-band slotted waveguide array antenna optimized using machine learning," *IEEE Antennas Wireless Propag. Lett.*, vol. 17, no. 11, pp. 2008–2012, Nov. 2018.

[14] L. Qin, Y. Lu, Q. You, Y. Wang, J. Huang, and P. Gardner, "Millimeter-wave slotted waveguide array with unequal beamwidths and low sidelobe levels for vehicle radars and communications," *IEEE Trans. Veh. Technol.*, vol. 67, no. 11, pp. 10574–10582, Nov. 2018.

[15] S.-G. Zhou, G.-L. Huang, T.-H. Chio, J.-J. Yang, and G. Wei, "Design of a wideband dual-polarization full-corporate waveguide feed antenna array," *IEEE Trans. Antennas Propag.*, vol. 63, no. 11, pp. 4775–4782, Nov. 2015.

[16] H. Yuan, J. Li, Z. Zhao, Z. Wang, M. Lodi, G. Gugliandolo, N. Donato, G. Crupi, L. Si, and X. Bao, "Development of a wideband slotted antenna array with low profile and low sidelobe," *Electronics*, vol. 12, no. 2, p. 278, Jan. 2023.

[17] E. Garcia-Marin, P. Sanchez-Olivares, J. L. Masa-Campos, J. A. Ruiz-Cruz, J. Herranz-Alpanseque, R. Garcia-Froilan, and F. Criado-Lopez, "Dual circularly polarized array antenna based on corporate feeding network in square waveguide technology," *IEEE Trans. Antennas Propag.*, vol. 69, no. 3, pp. 1763–1768, Mar. 2021.

[18] J. Wu, Y. J. Cheng, H. B. Wang, Y. C. Zhong, D. Ma, and Y. Fan, "A wideband dual circularly polarized full-corporate waveguide array antenna fed by triple-resonant cavities," *IEEE Trans. Antennas Propag.*, vol. 65, no. 4, pp. 2135–2139, Apr. 2017.

[19] H. Irie and J. Hirokawa, "Perpendicular-corporate feed in three-layered parallel-plate radiating-slot array," *IEEE Trans. Antennas Propag.*, vol. 65, no. 11, pp. 5829–5836, Nov. 2017.

[20] M. Farahani, M. Akbari, M. Nedil, A.-R. Sebak, and T. A. Denidni, "Millimeter-wave dual left/right-hand circularly polarized beamforming network," *IEEE Trans. Antennas Propag.*, vol. 68, no. 8, pp. 6118–6127, Aug. 2020.

[21] D. Zarifi, A. Farahbakhsh, A. U. Zaman, and P.-S. Kildal, "Design and fabrication of a high-gain 60-GHz corrugated slot antenna array with ridge gap waveguide distribution layer," *IEEE Trans. Antennas Propag.*, vol. 64, no. 7, pp. 2905–2913, Jul. 2016.

[22] M. Ferrando-Rocher, A. Valero-Nogueira, J. I. Herranz-Herruzo, and J. Teniente, "60 GHz single-layer slot-array antenna fed by groove gap waveguide," *IEEE Antennas Wireless Propag. Lett.*, vol. 18, no. 5, pp. 846–850, May 2019.

[23] M. Akbari, A. Farahbakhsh, and A.-R. Sebak, "Ridge gap waveguide multilevel sequential feeding network for high-gain circularly polarized array antenna," *IEEE Trans. Antennas Propag.*, vol. 67, no. 1, pp. 251–259, Jan. 2019.

[24] B. Zhang, Z. Zhan, Y. Cao, H. Gulan, P. Linnér, J. Sun, T. Zwick, and H. Zirath, "Metallic 3-D printed antennas for millimeter- and submillimeter wave applications," *IEEE Trans. THz Sci. Technol.*, vol. 6, no. 4, pp. 592–600, Jul. 2016.

[25] F. Bongard, M. Gimersky, S. Doherty, X. Aubry, and M. Krummen, "3D-printed Ka-band waveguide array antenna for mobile SATCOM applications," in *Proc. 11th Eur. Conf. Antennas Propag. (EUCAP)*, Mar. 2017, pp. 579–583.

[26] Z.-X. Xia, K. W. Leung, P. Gu, and R. Chen, "3-D-printed wideband high-efficiency dual-frequency antenna for vehicular communications," *IEEE Trans. Veh. Technol.*, vol. 71, no. 4, pp. 3457–3469, Apr. 2022.

[27] Y. Li, L. Ge, J. Wang, S. Da, D. Cao, J. Wang, and Y. Liu, "3-D printed high-gain wideband waveguide fed horn antenna arrays for millimeter-wave applications," *IEEE Trans. Antennas Propag.*, vol. 67, no. 5, pp. 2868–2877, May 2019.

[28] J. Rao, K. Nai, P. Vaitukaitis, Y. Li, and J. Hong, "Compact 3-D metal printed filtering antenna," *IEEE Antennas Wireless Propag. Lett.*, vol. 21, no. 2, pp. 386–390, Feb. 2022.

[29] P. G. Huray, O. Oluwafemi, J. Loyer, E. Bogatin, and X. Ye, "Impact of copper surface texture on loss: A model that works," *DesignCon*, vol. 1, pp. 462–483, Jun. 2010.
[30] M. Yi, S. Li, H. Yu, W. Khan, C. Ulusoy, A. Vera-Lopez, J. Papapolymerou, and M. Swaminathan, "Surface roughness modeling of substrate integrated waveguide in D-Band," *IEEE Trans. Microw. Theory Techn.*, vol. 64, no. 4, pp. 1209–1216, Apr. 2016.

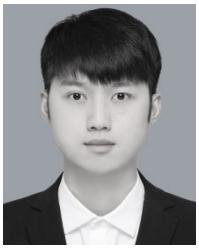

HAOYUN YUAN was born in Jiangxi, China, in 1999. He received the B.S. degrees in communication engineering from Jilin University, Changchun, China, in 2017 and 2021. He is currently pursuing the M.S. degree in electronic science and technology with the Beijing Institute of Technology, Beijing, China.

His current research interests include microwave measurement, machine learning, and waveguide slot antennas.

ZHUANGZHUANG LIU received the master's degree in materials engineering from the Central Iron and Steel Research Institute, Beijing, China, in 2013, and the Ph.D. degree in materials engineering from KU Leuven, Leuven, Belgium, in 2017.

He is currently an Associate Professor with the Institute for Advanced Materials and Technology, University of Science and Technology Beijing. His current research interests include design of electronic materials and additive manufacturing of multifunctional materials.

LI WANG (Graduate Student Member, IEEE) received the B.E. degree in information engineering from Xi'an Jiaotong University, Xi'an, China, in 2019, where he is currently pursuing the Ph.D. degree in electromagnetics and microwave technology.

His current research interests include radar nondestructive testing technology, ultrawideband time-domain imaging, and microwave ablation techniques.

LIMING SI (Member, IEEE) received the Ph.D. degree in electromagnetic field and microwave technology from the Beijing Institute of Technology (BIT), Beijing, China, in 2012.

He is currently an Associate Professor and the Vice Dean of the School of Integrated Circuits and Electronics, BIT. His research interests include electromagnetics, antennas, and metamaterials.

HOUJUN SUN (Member, IEEE) received the B.S., M.S., and Ph.D. degrees in electrical engineering from the Beijing Institute of Technology (BIT), Beijing, China, in 1991, 1994, and 1997, respectively.

He is currently a Professor with the School of Integrated Circuits and Electronics, BIT, where he is also with the Tangshan Research Institute. His research interests include integration technology of microwave/millimeter wave circuits and microwave imaging.

GIOVANNI CRUPI (Senior Member, IEEE) is currently an Associate Professor with the University of Messina, Messina, Italy. His main research interests include the characterization and modeling of microwave transistors for wireless applications and that of microwave sensors for bioengineering applications.

He is the Editor-in-Chief of the *International Journal of Numerical Modelling: Electronic Networks, Devices and Fields* (Wiley), the Section Editor-in-Chief of the *Electronics* (MDPI), and also an Associate Editor of the IEEE Microwave and Wireless Technology Letters and IEEE Access. He serves as a TPC Member for the IEEE INMMiC, TELSIKS, ICTA, and MMS Conferences and also the TPC Chair for the IEEE INMMiC, in 2014 and 2015. Since 2012, he has been the Chair of the IEEE MTT-S Graduate Fellowship Program.

DOMINIQUE SCHREURS (Fellow, IEEE) received the M.Sc. degree in electronic engineering and the Ph.D. degree from the University of Leuven (KU Leuven), Leuven, Belgium, in 1992 and 1997, respectively. She has been a Visiting Scientist with Agilent Technologies, Santa Rosa, CA, USA, ETH Zurich, Zurich, Switzerland, and the National Institute of Standards and Technology, Boulder, CO, USA. She is currently a Full Professor with KU Leuven, where she is also the Chair of the Leuven Centre on Information and Communication Technology (Leuven ICT). Her current research interests include the microwave and millimeter-wave characterization and modeling of transistors, nonlinear circuits, bioliquids, and system design for wireless communications and biomedical applications.

She served as the President for the IEEE Microwave Theory and Techniques Society, from 2018 to 2019. She was an IEEE MTT-S Distinguished Microwave Lecturer. She has also served as the General Chair for the Spring Automatic RF Techniques Group (ARFTG) Conferences, in 2007, 2012, and 2018, and the President of the ARFTG Organization, from 2018 to 2019. She also serves as the TPC Chair for the European Microwave Conference and also the Conference Co-Chair for the IEEE International Microwave Biomedical Conference. She was the Editor-in-Chief of the IEEE Transactions on Microwave Theory and Techniques.

XIUE BAO (Member, IEEE) received the Ph.D. degree in electrical engineering from KU Leuven, Leuven, Belgium, in 2020.

She is currently an Assistant Professor with the Beijing Institute of Technology (BIT), Beijing, China. She has been a Postdoctoral Researcher with KU Leuven and a Research Professor with Xi'an Jiaotong University (XJTU), Xi'an, China. Her current research interests include microwave and millimeter-wave technologies for biomedical, medical, and material applications, including measurement of broadband dielectric spectroscopy, sensor design, fabrication of microwave-microfluidic structure and flexible microwave devices, on-wafer measurement and vector network analyzer (VNA) calibration techniques within RF, microwave, millimeter wave, and terahertz frequency range.